Research Article Vol. 2, No. 10 / 15 October 2019 / OSA Continuum 2864

Resonant four-wave mixing microscopy on silicon-on-insulator based zero-contrast gratings

RABINDRA BISWAS,[1,2] JAYANTA DEKA,[1,2] KESHAV KUMAR JHA,[1] A. VISHNU PRAVEEN,[1] A. S. LAL KRISHNA,[1] SRUTI MENON,[1] AND VARUN RAGHUNATHAN[1,3]

[1]*Electrical Communications Engineering department, Indian Institute of Science, Bangalore, Karnataka 560012, India*
[2]*Equal contribution*
[3]*varunr@iisc.ac.in*

Abstract: In this paper, we report large area four-wave mixing microscopy studies on silicon-on-insulator based partially etched two-dimensional zero-contrast gratings. The zero-contrast gratings offer an additional degree of freedom for the design of spectral resonances by varying the etch depth of the grating structures. This is leveraged by designing signal resonance at 1580 nm, operating in the sub-wavelength, zeroth-order diffraction region and pump fixed at 1040 nm operating in the higher order diffraction region. The zero-contrast gratings are fabricated on standard 220 nm silicon-on-insulator substrates with etch depth chosen as 140 nm. The fabricated structures are characterized to measure the linear transmission and nonlinear four-wave mixing performance. Multi-spectral four-wave mixing images acquired across the grating structures for varying input signal wavelength show maximum enhancement of four-wave mixing signal at 1575 nm, with the on-grating four-wave mixing signal enhanced by ~ 450 times when compared to the un-patterned film. Zero-contrast gratings present a promising platform for realizing sub-wavelength scale nanostructured surfaces for nonlinear wave-mixing applications using standard silicon-on-insulator substrates. Such structures can find potential applications in wavelength conversion across widely separated wavelength bands and as substrates for nonlinear frequency conversion.

© 2019 Optical Society of America under the terms of the OSA Open Access Publishing Agreement

1. Introduction

Nonlinear optical effects in sub-wavelength scale structures is a promising area of research which is finding applications in small-scale sensing [1], switching [2], and wavelength conversion [3,4] devices. The inherent small interaction volume of such structures leads to low efficiency of the nonlinear optical process. To alleviate this problem, research has been directed towards enhancing the local excitation and emission fields using resonant electromagnetic modes in nanoscale geometries. For example, plasmonic structures have been widely used for this purpose to enhance harmonic generation and wave-mixing processes [5–7]. Though strong field confinement can be obtained from plasmonic structures, their lossy nature and low damage threshold limit their practical utility. Towards this end, dielectric nanostructures [8] offer a useful alternative to plasmonic structures, as they offer low loss, high damage threshold and field concentration inside the dielectric. Strong nonlinear response has been achieved in dielectric structures in the form of Mie scatterer exhibiting strong magnetic resonances in isolated and oligomeric form [9–11]. The collective modes of large arrays of dielectric structures in the form of high-contrast gratings exhibiting strong nonlinear response have also been reported [12,13].

Among the various of nonlinear optical processes studied in resonant nanostructures, Four-wave mixing (FWM) is an important process useful for performing wavelength conversion and is also

#372033 https://doi.org/10.1364/OSAC.2.002864
Journal © 2019 Received 23 Jul 2019; revised 11 Sep 2019; accepted 11 Sep 2019; published 27 Sep 2019

OSA CONTINUUM

utilized in micro-spectroscopy studies [4]. The non-degenerate FWM process is described as an optical wave mixing interaction between the input optical waves consisting of two pump fields (ω_{p1} and ω_{p2}) and one signal field (ω_s) resulting in the generation of the FWM field (ω_{FWM}) with frequency relationship given as [14]: $\omega_{FWM} = \omega_{p1} + \omega_{p2} - \omega_s$. The FWM process is termed degenerate FWM for the case of $\omega_{p1} = \omega_{p2} = \omega_p$. Degenerate FWM process has been studied in the past in silicon-based high contrast gratings [15] with pump and signal closely spaced in wavelength (~ 70 pm) within a single resonance. Germanium nanodisks that exhibit anapolar resonances have also been utilized for sum-frequency type wave-mixing processes with input wavelength separation of ~ 25 nm [16]. More recently, silicon nanodisks have been used to demonstrate doubly-resonant four-wave mixing by leveraging the first magnetic dipole and second electric dipole resonance with ~ 350 nm separation between the input wavelengths [17]. In these previous reports, spatially resolved studies of the resonant FWM through microscopic imaging has not been reported.

In the present paper, we report FWM studies due to collective resonant electromagnetic modes in silicon-on-insulator (SOI) based partially etched two-dimensional zero-contrast gratings (ZCGs). ZCGs consist of partially etched high-index grating structures with the thickness of the unetched layer providing an additional degree of freedom to design robust spectral responses from such structures [18]. The ability to tune the resonance in the ZCGs by varying the un-etched layer thickness is demonstrated using simulations. The ZCGs are designed to support a prominent resonance at the signal wavelength in the zeroth order diffraction regime (at ~ 1580 nm) with the pump wavelength showing moderate field enhancement in the higher order diffraction region (at ~ 1040 nm) resulting in four-wave mixing at ~ 775 nm. Spatially resolved FWM microscopy images of the fabricated ZCG structure is presented and the FWM signal is found to be resonantly enhanced on the grating by ~ 450 times when compared to the un-patterned silicon layer. The FWM process is further characterized using power, polarization and temporal dependence studies. The sub-wavelength thickness of the silicon-on-insulator platform and the ability to tune the fundamental resonance during fabrication by varying the etch depth allows the realization of a versatile FWM source at the nanoscale. The wide separation between the pump and signal or pump and FWM (~ 100 THz) as employed here is particularly useful for applications in wavelength-conversion across widely separated spectral bands and as substrates for nonlinear wave-mixing studies.

2. Design studies

The top and side view schematics of the periodically arranged ZCG structures under study are shown in Fig. 1(a) and (b) respectively. It consists of a silicon substrate with 2000 nm thick buried-oxide film followed by the ZCG structure. The ZCG is arranged in a two-dimensional hexagonal lattice with the XYZ axes representing the lab co-ordinates. The top silicon layer has a total thickness H = 220 nm, of which thickness of the un-etched silicon layer is h. The un-etched silicon layer thickness, in addition to the pitch, Λ and structure diameter, D provides the degrees of freedom required to tailor the resonances of the ZCG. The simulation studies of the ZCG structures are performed using Lumerical Finite Difference Time Domain (FDTD) software [19]. The transmission contour map obtained is shown in Fig. 1(c) for normal incidence plane wave excitation as a function of varying etch depth, H-h. The hexagonal array pitch and diameter are fixed as 1200 nm and 660 nm respectively for this study. The black dashed vertical line shows the separation between the sub-wavelength regime or zeroth diffraction orders regime and the higher diffraction orders regimes at ~ 1540 nm, representing the wavelength for the onset of diffraction in the buried oxide layer (given as: $\frac{\sqrt{3}}{2}\Lambda.n_{oxide}$ [20]). The resonance features observed for the ZCG structures can be explained based on the guided-mode resonance phenomena in diffraction gratings and high index unetched guiding layer [21]. The transmission spectrum for three different etch depths (20 nm, 140 nm and 220 nm) are plotted in Fig. 1(d) showing the signal

OSA CONTINUUM

and pump spectral regions. Sharp resonances can be observed in the sub-diffraction region for lower etch depths, which broaden and shift to shorter wavelengths with increasing etch depth. For fully etched structures, a second resonance also starts appearing in the longer wavelength region. The resonances in the higher order diffraction region do not show similar sharpness as seen in the signal spectrum, and hence field enhancements at the pump wavelength are expected to be weaker. By choosing an appropriate etch depth, the resonance wavelength and its spectral width can be engineered, thus underscoring the additional degree of freedom available in ZCG structures.

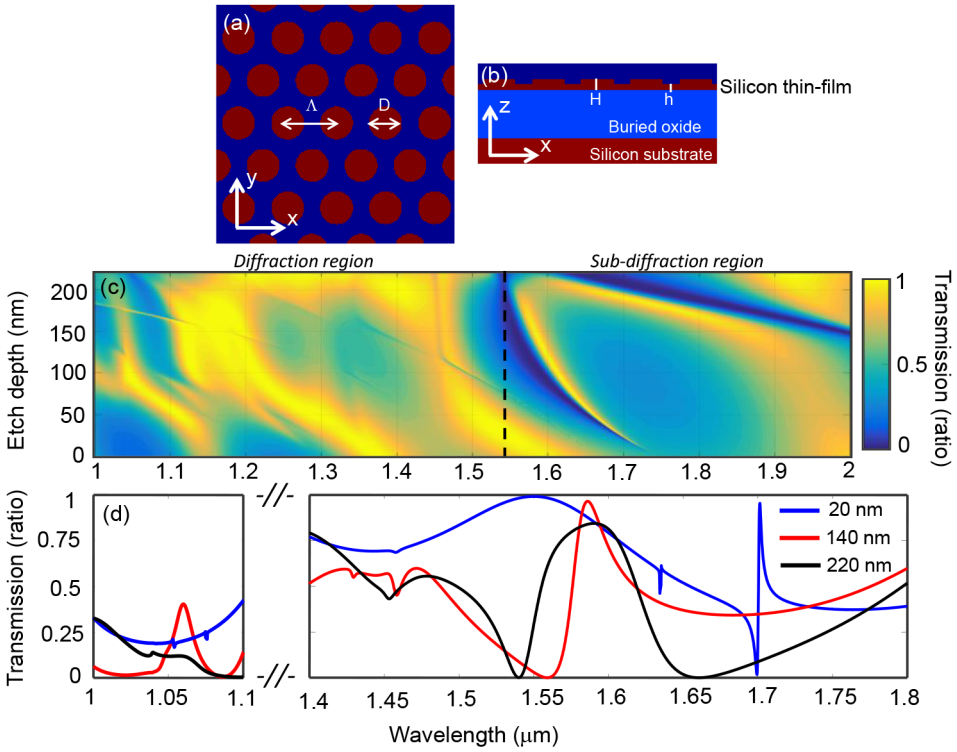

Fig. 1. (a) Top-view and (b) side-view of the ZCG structures with the Cartesian axis shown. (c) Transmission contour as a function of the incident wavelength and varying etch depth, H-h for the ZCG. (d) The line profile of the transmission spectrum shown for three different etch depths and wavelength ranges of 1 to 1.1 μm and 1.4 to 1.8 μm.

The simulated electric field profiles for both pump and signal wavelengths are shown in Fig. 2(a) and (b) respectively for X-polarized incident plane waves and fixed etch depth of 140 nm. This etch depth is chosen to get the signal resonance in the 1550-1600 nm region. For this etch depth, the resonance at the signal wavelength was found to be located at 1580 nm and the pump wavelength is fixed at 1040 nm. For the incident light polarization along X for both pump and signal fields, X and Z component of electric fields are found to be enhanced, while Y component is found to be negligible. At the signal wavelength, significant field enhancement (~ 13 times) is observed inside the silicon structure along the longitudinal direction (Z component). In comparison, the field at the pump wavelength for the X component is modestly enhanced (< 4.5 times), due to the weak resonance obtained at ~ 1060 nm, as shown in Fig. 1(d). FWM nonlinear polarization components at the frequency of $2\omega_p$-ω_s can be expanded in terms of the

OSA CONTINUUM

field profile inside the ZCG structure and the nonlinear optical susceptibility as:

$$P^{(3)}_{FWM-x} = \varepsilon_o \left(\begin{array}{c} \chi^{(3)}_{xxxx} E^2_{px} E^*_{sx} + 2\chi^{(3)}_{xxyy} E_{px} E_{py} E^*_{sy} + 2\chi^{(3)}_{xxyy} E_{px} E_{pz} E^*_{sz} \\ + \chi^{(3)}_{xyyx} E^2_{py} E^*_{sx} + \chi^{(3)}_{xyyx} E^2_{pz} E^*_{sx} \end{array} \right) \quad (1)$$

$$P^{(3)}_{FWM-y} = \varepsilon_o \left(\begin{array}{c} \chi^{(3)}_{xxxx} E^2_{py} E^*_{sy} + 2\chi^{(3)}_{xxyy} E_{py} E_{px} E^*_{sx} + 2\chi^{(3)}_{xxyy} E_{py} E_{pz} E^*_{sz} \\ + \chi^{(3)}_{xyyx} E^2_{px} E^*_{sy} + \chi^{(3)}_{xyyx} E^2_{pz} E^*_{sy} \end{array} \right) \quad (2)$$

$$P^{(3)}_{FWM-z} = \varepsilon_o \left(\begin{array}{c} \chi^{(3)}_{xxxx} E^2_{pz} E^*_{sz} + 2\chi^{(3)}_{xxyy} E_{pz} E_{py} E^*_{sy} + 2\chi^{(3)}_{xxyy} E_{pz} E_{px} E^*_{sx} \\ + \chi^{(3)}_{xyyx} E^2_{py} E^*_{sz} + \chi^{(3)}_{xyyx} E^2_{px} E^*_{sz} \end{array} \right) \quad (3)$$

where, E_{ij}, with i = p,s and j = x,y,z represents the three components of the electric field at the pump and stokes wavelengths. It is assumed that the lab-coordinate align with the crystallographic axis of the silicon lattice, which can be set during the structure fabrication and experimental characterization. The symmetry properties of the third-order nonlinear optical susceptibility of silicon are applied above with the non-zero optical susceptibilities elements of the form [14]: $\chi^{(3)}_{1111}$, $\chi^{(3)}_{1122}$, $\chi^{(3)}_{1221}$, $\chi^{(3)}_{1212}$ with subscripts 1,2 taking values x,y, or z. The $\chi^{(3)}_{1111}$ term has the largest magnitude and when Kleinman symmetry is applicable the cross-terms can be written as: $\chi^{(3)}_{1122} \approx \chi^{(3)}_{1221} \approx \chi^{(3)}_{1212} \approx r\chi^{(3)}_{1111}$ [14], with the values of ratio, r reported in the range of 0.48 to 0.62 [22,23]. However, Kleinman symmetry may not be applicable for the wavelengths under

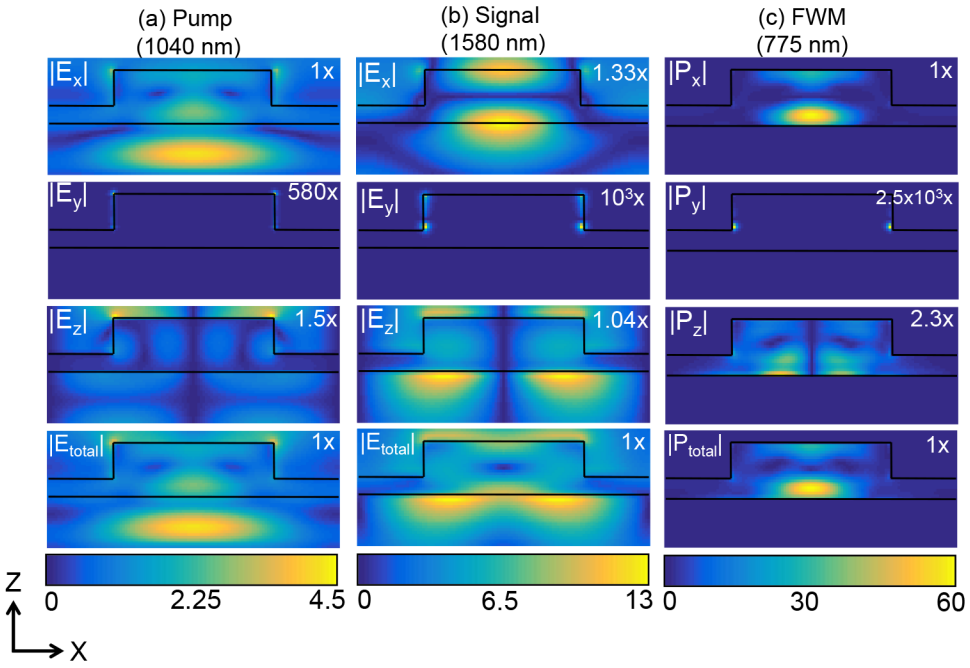

Fig. 2. Cross sectional field profiles at: (a) pump field – 1040 nm, (b) signal resonance field – 1580 nm and (c) nonlinear polarization at 775 nm. X, Y, Z components and total absolute value are shown in the figures with the Z-X cross-sectional profiled. The dimension of the ZCG used for these simulations are: Λ = 1.2 μm, D = 660 nm, H = 220 nm and h = 80 nm. The multiplication factor used to get the magnitude of the fields to the same range, as indicated by the colorbar below the respective columns is shown in the figures.

OSA CONTINUUM

consideration in this work. The strength of the nonlinear polarization is strongly dependent on the overlap of the pump and signal field profiles inside the structure, thus resulting in the significant term in the above equations being $\varepsilon_o \chi^{(3)}_{xxxx} E^2_{px} E^*_{sx}$ for X-polarized incident fields. The nonlinear polarization components at the FWM wavelength of 775 nm are also shown in Fig. 2(c), with the X component enhanced by ~ 60 times.

Next, the angular dependence of the ZCG transmission spectrum is shown in Fig. 3. The structures are designed to operate optimally close to normal incidence, and the resonance peak is found to shift to the longer wavelength side and narrow in spectral width with increasing angle. The resonance peak is found to shift from 1580 nm to 1650 nm with ~ 8° change in the incidence angle. In the context of performing nonlinear microscopy studies, the use of high numerical aperture optics to create large optical intensity at the focus leads naturally to the excitation of the sample at varying incidence angle [24]. The use of 100 s of fsec wide pulses as incident laser beams with typical spectral widths of 20-30 nm can benefit from the multi-angle excitation to some extent, as the broad incident laser spectrum can excite the full resonance spectrum of the structure.

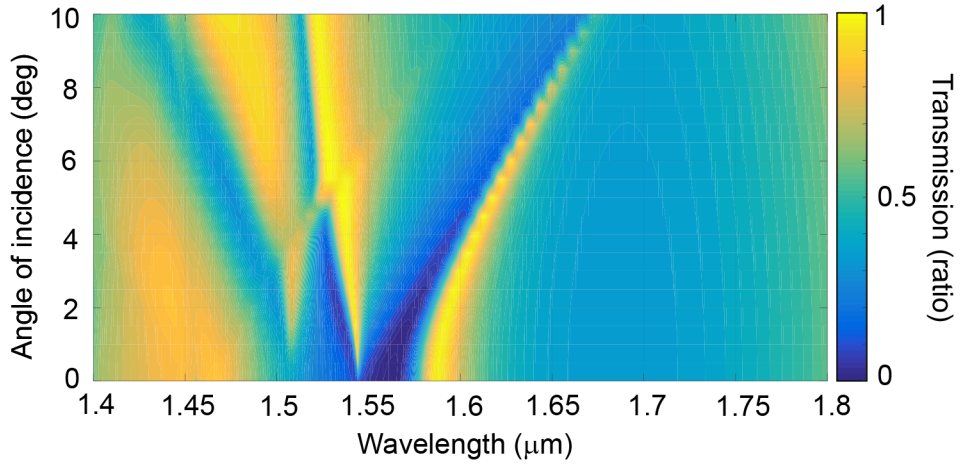

Fig. 3. The transmission contour shown as a function of the signal wavelength (x-axis) and angle-of-incidence (y-axis) with respect to the normal. The dimension of the ZCG used for these simulations are: Λ = 1200 nm, D = 660 nm, H = 220 nm and h = 80 nm.

3. Fabrication

The ZCG structures are fabricated on a [1 0 0] SOI wafer with a top silicon layer of thickness of H = 220 nm, as used in the simulations with buried oxide layer of thickness 2000 nm on a silicon substrate of ~ 500 μm thickness. The hexagonal array of nanodisks is patterned using electron-beam lithography, followed by pattern transfer using fluorine-based plasma dry etching. The scanning electron microscopy (SEM) and atomic force microscopy (AFM) images of the fabricated structure are shown in Fig. 4(a) and (b) respectively. The fabricated structures have the following dimensions: Λ = 1200 nm, D = 660 nm and H-h = 140 nm.

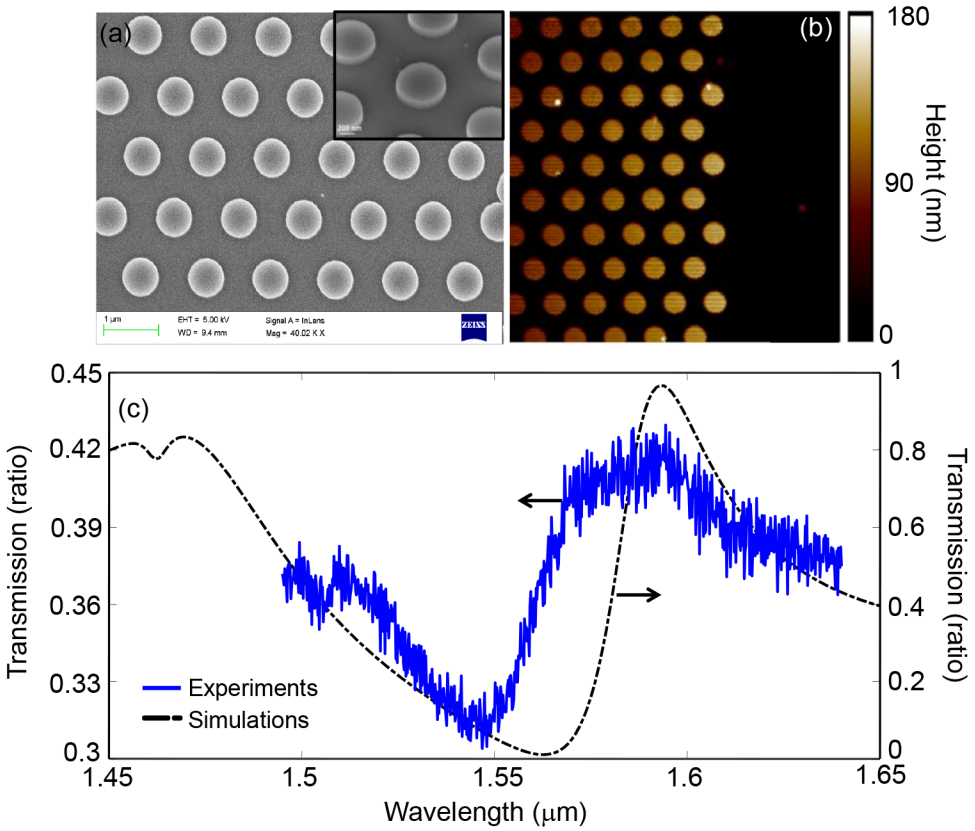

Fig. 4. (a) SEM image, (b) AFM image of the fabricated ZCG structures with field of view of $7 \times 5\,\mu m$ and $10 \times 10\,\mu m$ respectively. (c) Transmission spectrum obtained for the fabricated ZCG structure. Blue curve (left axis) corresponds to experiments and the black curve (right axis) corresponds to simulations. The fabricated device dimensions are: $\Lambda = 1200$ nm, D = 660 nm and etch depth = 140 nm.

4. Experimental studies

The linear transmission measurements are performed using an Agilent external cavity tunable laser source with a tuning range of 1495 nm to 1640 nm. The linear transmission measurement results are shown in Fig. 4(c). A schematic of the experimental set-up used for both linear and nonlinear measurements is shown in Fig. 5. The laser beam is loosely focused on the ZCG structures with a low numerical aperture (0.1 NA) objective lens and the transmitted light is detected using a Germanium photodetector. The on-grating transmission signal is normalized with respect to a reference glass slide. The experimentally obtained transmission spectrum is compared with the simulated spectrum obtained with similar device dimensions. Good agreement between the resonance profiles is observed, with the simulation curve found to be slightly red-shifted with respect to the experimental plot. The experimental plot also shows reduced contrast, which is attributed to the fabrication imperfections leading to rough surfaces and nanodisk sidewalls. The range of excitation angles used for this measurement (~ 0-10°) also lead to discrepancies when compared to the normal incidence simulation results.

The FWM studies are performed using a nonlinear optical microscopy system as shown in the experimental setup in Fig. 5. The incident laser sources consist of a pump fiber laser (Fidelity HP) operating at 1040 nm with a pulse width of 140 fsec and a repetition rate of 80 MHz. The

OSA CONTINUUM

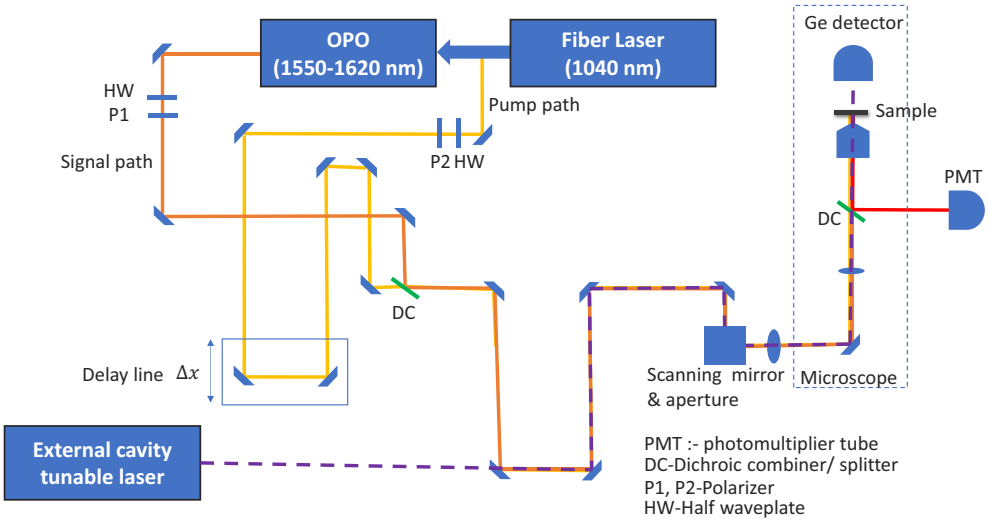

Fig. 5. The schematic of the experimental setup used for linear transmission and nonlinear four-wave mixing experiments.

signal laser is an optical parametric oscillator (Levante IR) pumped by the above pump laser resulting in pulse width of 200 fsec and used here in the near infrared wavelength range of 1550 to 1620 nm range. The pump and signal sources are self-synchronized as they are derived from the same fiber laser source. The pump and the signal laser are combined using a set of mirrors with time delay adjusted using a motorized stage (Thorlabs KDC101), combined using dichroic beam combiner and aligned together to get maximum spatial overlap. The pump and signal beams are focused on the sample using a 20x/0.75 NA objective. The same objective is used to collect the generated FWM in the backward direction and separated from the excitation using a dichroic splitter. The FWM signal is then detected using a photomultiplier tube (Hamamatsu R2658 PMT) with a set of bandpass (785nm ± 20nm) and short pass (890nm) filters mounted in front to reject the pump and signal reflected light. A pair of galvanometric mirrors (Thorlabs GVS002) is used to scan the laser beam to obtain the two-dimensional FWM images of the sample. For the imaging experiments, the angle of illumination after focusing is restricted using an aperture placed close to the scanning mirror pivot point at the conjugate plane to the back focal plane of the objective lens. The aperture restricts the incident light to 40% of the full back aperture diameter of the objective, thus resulting in maximum acceptance angle of 19°.

The detected nonlinear signal is verified to be FWM using incident power dependence as shown in Fig. 6(a). The input power and the generated nonlinear signal (shown as PMT voltage) are plotted in a log-log plot exhibiting slopes of 1.06 and 2.19 as a function of signal and pump power respectively. We also performed polarization dependence studies by rotating the incident signal polarization, keeping the pump X-polarized and collecting the FWM signal without any analyzer before the PMT (i.e. simultaneously collecting output polarized both parallel and perpendicular to the lab co-ordinates). The input polarization dependent FWM signal shown in Fig. 6(b), exhibiting an oblong double-lobed profile. The simulated data shown in Fig. 6(b) is obtained by rotating the incident signal polarization keeping the pump X-polarized and calculating the nonlinear polarization. We compare the experimental data with the simulated maximum nonlinear polarization intensity: $\max(|P_x^{(3)}|^2 + |P_y^{(3)}|^2 + |P_z^{(3)}|^2)$- normalizing the peak to the maximum of the experimental data. This quantity represents approximately the FWM signal generated at the sample, and hence proportional to the detected far-field FWM signal at the detector plane. The

OSA CONTINUUM

two significant nonlinear polarization components with the incident signal polarization rotated in the XY plane are found to be: $P_x^{(3)} = \varepsilon_o \chi_{xxxx}^{(3)} E_{px}^2 E_{sx}^*$ and $P_y^{(3)} = \varepsilon_o \chi_{xyyx}^{(3)} E_{px}^2 E_{sy}^*$. Good agreement between the experimental data and the simulated fit is obtained when the ratio, $r = \frac{\chi_{xyyx}^{(3)}}{\chi_{xxxx}^{(3)}}$ takes a value of 0.75. For comparison, simulated plot for the case of r = 0.5 is also shown in Fig. 6(b).

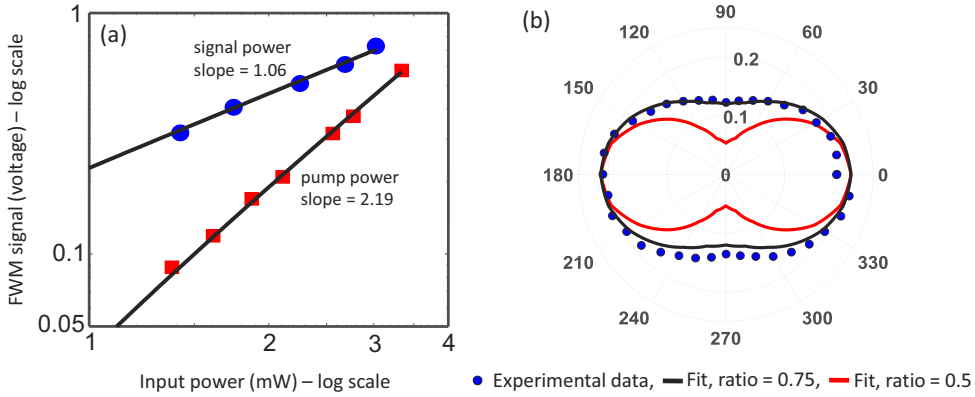

Fig. 6. (a) Power dependence of the FWM signal (measured as PMT voltage) as a function of the input signal and pump power level. (b) The dependence of FWM signal (shown as PMT voltage) as a function of the input signal polarization rotated in the XY plane. The experimental data is shown by blue circles and simulated fit to the data is the maximum nonlinear polarization intensity – normalized to the peak experimental data. The black and red simulated fit corresponds to two different nonlinear susceptibility ratios, r = 0.75 and 0.5 respectively.

For the spatially-resolved FWM microscopy studies, incident optical power of 9 mW and 7 mW are used at the pump and signal wavelengths respectively. A series of FWM microscopy images obtained as a function of the time delay between the signal and pump pulses is shown in Fig. 7. The FWM signal is found to be sensitive to the temporal overlap between the pump and signal and is found to decreases sharply as a function of the time-delay as set by the motorized stage. Figure 8 shows the large field-of-view and multi-spectral imaging capability of the FWM microscopy system. FWM microscopy images across an area of 300×300 μm was acquired at an optical resolution of ~ 1.3 μm. This field-of-view includes spatially distributed FWM signal across ~ 20,000 nanodisks in the hexagonal array. Multi-spectral FWM images of ZCGs are obtained by tuning the signal OPO from 1550 to 1620 nm. Figure 8(b)–(g) shows the FWM images taken for different wavelength as labeled in the figure. Figure 8(h) shows the comparison of the average FWM signal (shown as PMT voltage) both on and off the ZCG structure as a function of the signal wavelength. Enhanced FWM signal is observed in the on-grating region throughout the wavelength range of interest with the maximum enhancement factor of ~450 obtained for the signal wavelength of 1575nm, which is very close to the resonance observed in the linear transmission measurements. The overall FWM conversion efficiency on-resonance is estimated to be ~ 10^{-7}%, taking into account the path loss from the sample plane to the PMT and response of the PMT. In the present study, no particular attention was paid to optimizing the pump resonance and the only the single signal resonance was carefully designed. Further enhancement in the FWM signal and conversion efficiency can be attained using doubly-resonant designs with field enhancement for both incident pump and signal wavelengths [17], and by improving the quality factor of the resonant structures through fabrication optimization.

OSA CONTINUUM

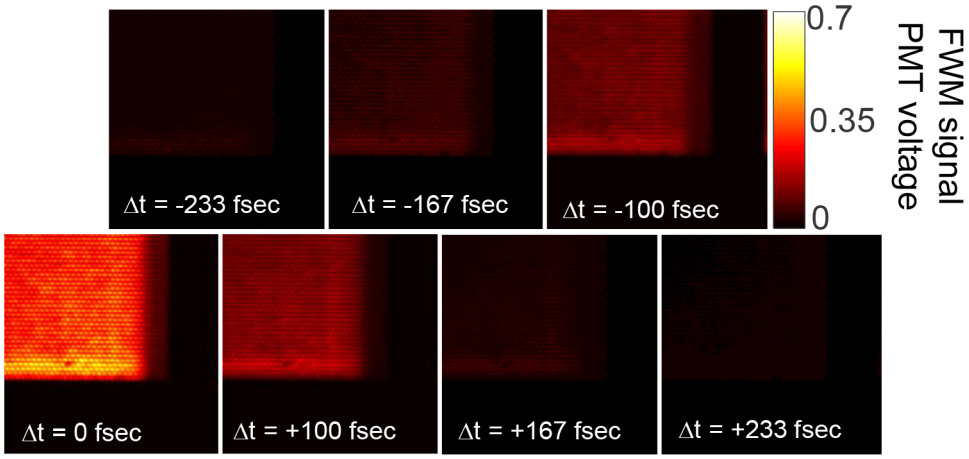

Fig. 7. FWM microscopy images as a function of time delay, Δt between the input pump and signal laser pulses. The image field-of-view is of size 100 × 100 μm.

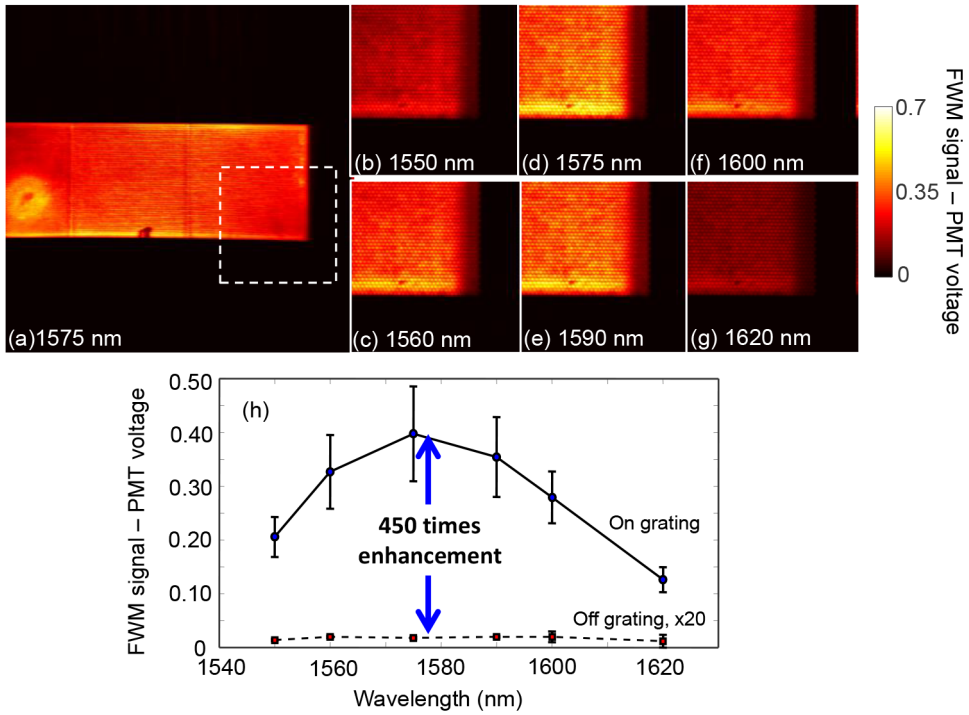

Fig. 8. (a) Four-wave mixing microscopy image (shown as PMT voltage) at 1575 nm signal wavelength with large field-of-view of 300 × 300 μm. Multi-spectral FWM microscopy images acquired at input signal wavelengths of: (b) 1550 nm, (c) 1560 nm, (d) 1575 nm, (e) 1590 nm, (f) 1600 nm and (g) 1620 nm. Field-of-view for the multispectral imaging is 100 × 100 μm. (h) Comparison of average FWM signals both on- and off- gratings as a function of the input signal wavelengths used in multispectral studies. Maximum resonant enhancement of 450 is observed.

OSA CONTINUUM

5. Conclusions

In this paper, we report resonant four-wave mixing microscopy studies on SOI based 2D ZCGs. In comparison to guided-mode resonance structures and high contrast gratings, ZCGs provide one more degree of freedom in terms of the etch depth to optimize the supported spectral resonances. This is leveraged in this work to place the resonance of the ZCG in the 1550 to 1600 nm wavelength region, corresponding the incident signal resonance in the zeroth order diffraction region with ~ 13 times enhancement in the field. The incident pump operates in the higher order diffraction region with a modest field enhancement of 4.5 times. Degenerate FWM microscopy of the ZCG structure is performed to obtain large field-of-view (300×300 μm) images of the structure on-resonance and also perform multi-spectral imaging studies. The FWM process is found to be resonantly enhanced at 1575 nm with the FWM signal on-grating showing ~ 450 times enhancement when compared to the un-patterned film. The power, polarization and temporal dependence of the FWM are also presented. The sub-wavelength thickness of the SOI platform and the ability to tune the fundamental resonance during fabrication by varying the etch depth allows the realization of a versatile FWM source at the nanoscale using ZCG structures. Further improvement in FWM resonance enhancement can be obtained by designing doubly-resonant structures with resonances supported for both the pump and signal wavelengths. Such sub-wavelength scale nonlinear optical surfaces can potentially find applications in wavelength conversion across widely separated spectral bands [25] and as substrates for nonlinear wave-mixing studies [26].

Funding

Science and Engineering Research Board; Indian Space Research Organisation; Nano Mission Council, Department of Science and Technology; Ministry of Electronics and Information technology; Ministry of Human Resource Development.

References

1. J. Butet, I. Russier-Antoine, C. Jonin, N. Lascoux, E. Benichou, and P.-F. Brevet, "Sensing with Multipolar Second Harmonic Generation from Spherical Metallic Nanoparticles," Nano Lett. **12**(3), 1697–1701 (2012).
2. M. R. Shcherbakov, P. P. Vabishchevich, A. S. Shorokhov, K. E. Chong, D.-Y. Choi, I. Staude, A. E. Miroshnichenko, D. N. Neshev, A. A. Fedyanin, and Y. S. Kivshar, "Ultrafast All-Optical Switching with Magnetic Resonances in Nonlinear Dielectric Nanostructures," Nano Lett. **15**(10), 6985–6990 (2015).
3. S. V. Makarov, A. N. Tsypkin, T. A. Voytova, V. A. Milichko, I. S. Mukhin, A. V. Yulin, S. E. Putilin, M. A. Baranov, A. E. Krasnok, I. A. Morozov, and P. A. Belov, "Self-adjusted all-dielectric metasurfaces for deep ultraviolet femtosecond pulse generation," Nanoscale **8**(41), 17809–17814 (2016).
4. Y. Wang, C.-Y. Lin, A. Nikolaenko, V. Raghunathan, and E. O. Potma, "Four-wave mixing microscopy of nanostructures," Adv. Opt. Photonics **3**(1), 1–52 (2011).
5. J. Butet, P.-F. Brevet, and O. J. F. Martin, "Optical Second Harmonic Generation in Plasmonic Nanostructures: From Fundamental Principles to Advanced Applications," ACS Nano **9**(11), 10545–10562 (2015).
6. H. Aouani, M. Rahmani, M. Navarro-Cía, and S. A. Maier, "Third-harmonic-upconversion enhancement from a single semiconductor nanoparticle coupled to a plasmonic antenna," Nat. Nanotechnol. **9**(4), 290–294 (2014).
7. Y. Zhang, F. Wen, Y.-R. Zhen, P. Nordlander, and N. J. Halas, "Coherent Fano resonances in a plasmonic nanocluster enhance optical four-wave mixing," Proc. Natl. Acad. Sci. U. S. A. **110**(23), 9215–9219 (2013).
8. A. I. Kuznetsov, A. E. Miroshnichenko, M. L. Brongersma, Y. S. Kivshar, and B. Lukyanchuk, "Optically resonant dielectric nanostructures," Science **354**(6314), aag2472 (2016).
9. M. R. Shcherbakov, D. N. Neshev, B. Hopkins, A. S. Shorokhov, I. Staude, E. V. Melik-Gaykazyan, M. Decker, A. A. Ezhov, A. E. Miroshnichenko, I. Brener, A. A. Fedyanin, and Y. S. Kivshar, "Enhanced Third-Harmonic Generation in Silicon Nanoparticles Driven by Magnetic Response," Nano Lett. **14**(11), 6488–6492 (2014).
10. Y. Yang, W. Wang, A. Boulesbaa, I. I. Kravchenko, D. P. Briggs, A. Puretzky, D. Geohegan, and J. Valentine, "Nonlinear Fano-Resonant Dielectric Metasurfaces," Nano Lett. **15**(11), 7388–7393 (2015).
11. M. R. Shcherbakov, A. S. Shorokhov, D. N. Neshev, B. Hopkins, I. Staude, E. V. Melik-Gaykazyan, A. A. Ezhov, A. E. Miroshnichenko, I. Brener, A. A. Fedyanin, and Y. S. Kivshar, "Nonlinear Interference and Tailorable Third-Harmonic Generation from Dielectric Oligomers," ACS Photonics **2**(5), 578–582 (2015).
12. C. J. Chang-Hasnain and W. Yang, "High-contrast gratings for integrated optoelectronics," Adv. Opt. Photonics **4**(3), 379–440 (2012).
13. J. Deka, K. K. Jha, S. Menon, A. S. L. Krishna, R. Biswas, and V. Raghunathan, "Microscopic study of resonant third-harmonic generation from amorphous silicon nanodisk arrays," Opt. Lett. **43**(21), 5242–5245 (2018).

OSA CONTINUUM

14. J. M. Liu, *Photonic Devices*, 1st ed. (Cambridge Univ. Press, 2005), chap. 9.
15. T. Sun, W. Yang, and C. J. Chang-Hasnain, "Surface-normal coupled four-wave mixing in a high contrast gratings resonator," Opt. Express **23**(23), 29565–29572 (2015).
16. G. Grinblat, Y. Li, M. P. Nielsen, R. F. Oulton, and S. A. Maier, "Degenerate Four-Wave Mixing in a Multiresonant Germanium Nanodisk," ACS Photonics **4**(9), 2144–2149 (2017).
17. R. Colom, L. Xu, L. Marini, F. Bedu, I. Ozerov, T. Begou, J. Lumeau, A. E. Miroshnishenko, D. Neshev, B. T. Kuhlmey, S. Palomba, and N. Bonod, "Enhanced Four-Wave Mixing in Doubly Resonant Si Nanoresonators," ACS Photonics **6**(5), 1295–1301 (2019).
18. R. Magnusson, "Wideband reflectors with zero-contrast gratings," Opt. Express **39**(15), 4337–4340 (2014).
19. Lumerical FDTD: https://www.lumerical.com/products/fdtd/
20. P. Qiao, L. Zhu, W. Cho Chew, and C. J. Chang-Hasnain, "Theory and design of two-dimensional high-contrast-grating phased arrays," Opt. Express **23**(19), 24508–24524 (2015).
21. S. S. Wang and R. Magnusson, "Theory and applications of guided-mode resonance filters," Appl. Opt. **32**(14), 2606–2613 (1993).
22. J. J. Wynne, "Optical Third-Order Mixing in GaAs, Ge, Si, and InAs," Phys. Rev. **178**(3), 1295–1303 (1969).
23. W. Y. Ching and M.-Z. Huang, "Calculation of optical excitation in cubic semiconductors. III. Third harmonic generation," Phys. Rev. B **47**(15), 9479–9491 (1993).
24. L. Novotny, *Principles of Nano-Optics*, 2nd ed. (Cambridge Univ. Press, 2012), chap. 4.
25. V. Raghunathan, R. Claps, D. Dimitropoulos, and B. Jalali, "Parametric Raman wavelength conversion in scaled silicon waveguides," J. Lightwave Technol. **23**(6), 2094–2102 (2005).
26. E. O. Potma, C. L. Evans, and X. S. Xie, "Heterodyne coherent anti-Stokes Raman scattering (CARS) imaging," Opt. Lett. **31**(2), 241–243 (2006).

14.139.126.34 on 2022-10-13 02:46:57